Naval Research Laboratory
Washington, DC 20375-5320

NRL/7530/FR--2024/6

Impact of Assimilating COWVR in the Navy's Global Numerical Model

H. CHRISTOPHERSEN
S. SWADLEY

Atmospheric Dynamics and Prediction
Marine Meteorology

E. SIMON

SAIC

W. CAMPBELL

Atmospheric Dynamics and Prediction
Marine Meteorology

S. BROWN

Jet Propulsion Laboratory

E. SATTERFIELD

Atmospheric Dynamics and Prediction
Marine Meteorology

S. FARRAR
The Aerospace Corporation

June 24, 2024

REPORT DOCUMENTATION PAGE

PLEASE DO NOT RETURN YOUR FORM TO THE ABOVE ORGANIZATION.

1. REPORT DATE	2. REPORT TYPE	3. DATES COVERED	
		START DATE	END DATE
June 24, 2024	NRL Formal Report	October 1, 2023	June 1, 2024

4. TITLE AND SUBTITLE

Impact of Assimilating COWVR in the Navy's Global Numerical Model

5a. CONTRACT NUMBER	5b. GRANT NUMBER	5c. PROGRAM ELEMENT NUMBER
		100002064048 0010
5d. PROJECT NUMBER	**5e. TASK NUMBER**	**5f. WORK UNIT NUMBER**
		996D52

6. AUTHOR(S)

H. Christophersen, S. Swadley, E. Simon, W. Campbell, S. Brown, E. Satterfield, and S Farrar

7. PERFORMING ORGANIZATION NAME(S) AND ADDRESS(ES)	8. PERFORMING ORGANIZATION REPORT NUMBER
U.S. Naval Research Laboratory, Marine Meteorology Division 7 Grace Hopper Ave, Monterey, CA 93943	NRL/7530/FR--2024/6

9. SPONSORING/MONITORING AGENCY NAME(S) AND ADDRESS(ES)	10. SPONSOR/MONITOR'S ACRONYM(S)	11. SPONSOR/MONITOR'S REPORT NUMBER(S)
U.S. Naval Research Laboratory 4555 Overlook Ave, Washington, DC 20375	NRL	IR-7531-24-1-U

12. DISTRIBUTION/AVAILABILITY STATEMENT

Distribution Statement A: Approved for public release. Distribution is unlimited.

13. SUPPLEMENTARY NOTES

14. ABSTRACT

This work assimilates the Compact Ocean Wind Vector Radiometer (COWVR) clear-sky radiances and evaluate their influence on the Navy's global numerical weather prediction system. COWVR assimilation in NAVGEM shows a comparable positive impact on the 24-h model forecasts to that of legacy microwave sensors. Furthermore, the assimilation of COWVR radiances demonstrates a substantial positive impact on wind forecasts beyond the 72-h lead-time, particularly in the Tropics and Southern Hemisphere.

15. SUBJECT TERMS

Compact Ocean Wind Vector Radiometer (COWVR), Polarimetric radiometer, data assimilation, numerical weather prediction

16. SECURITY CLASSIFICATION OF:			17. LIMITATION OF ABSTRACT	18. NUMBER OF PAGES
a. REPORT	b. ABSTRACT	C. THIS PAGE		
U	U	U	UU	30

19a. NAME OF RESPONSIBLE PERSON	19b. PHONE NUMBER *(Include area code)*
Hui Christophersen (7531)	831-656-4027

PREVOUS EDITION IS OBSOLETE

STANDARD FORM 298 (REV. 5/2020)
Prescribed by ANSI Std. Z39.18

This page intentionally left blank

CONTENTS

FIGURES

This page intentionally left blank

EXECUTIVE SUMMARY

As a technology demonstration for the Department of Defense Space Test program - Houston 8 (STP-H8), the Compact Ocean Wind Vector Radiometer (COWVR) efficiently retrieves ocean surface vector winds, precipitation, and cloud liquid water at a fraction of the cost of legacy passive microwave (MW) sensors. COWVR measurements are fully polarimetric at lower microwave (MW) frequencies (18.7 GHz, 23.8 GHz, and 33.9 GHz), allowing them to provide valuable forward (fore) and rear (aft) looks at the same Earth scene, which is useful for the detection of potential radio frequency interference from geostationary satellites. The primary objective of this study is to assimilate COWVR clear-sky radiances and to evaluate their influence on global numerical weather prediction (NWP). COWVR assimilation in the Navy Global Environmental Model (NAVGEM) shows a comparable positive impact on the 24-h model forecasts to that of legacy MW sensors. Furthermore, the assimilation of COWVR radiances demonstrates a substantial positive impact on wind forecasts beyond the 48-h lead time, particularly in the Tropics and the Southern Hemisphere (0.5–1.25% enhancement in wind forecast accuracy).

As the Global Observing System continues to evolve, smaller satellites are emerging as cost-effective alternatives for delivering crucial Earth observations. One of the primary challenges facing the NWP community is to validate the capability of small satellites (SmallSats) to provide high-quality Earth observations despite their much smaller size and cost. This study initiates an exploration of the assimilation of COWVR radiance data into the Navy's global NWP model, with a focus on evaluating their influence on NWP analyses and forecasts. The results show comparable performance to legacy MW sensors and performance enhancement for wind forecasts at 48-hour-and-longer lead times. This enhanced impact, particularly in longer-term wind forecasting, stands out as a significant outcome of this study.

This page intentionally left blank

IMPACT OF ASSIMILATING COWVR IN THE NAVY'S GLOBAL NUMERICAL MODEL

1 INTRODUCTION

As part of a collaborative mission developed jointly by the Jet Propulsion Laboratory and sponsored by the U.S. Space Force Space Systems Command, the Department of Defense Space Test Program - Houston 8 (STP-H8) is a three-year initiative designed to showcase innovative, cost-effective MW radiometers for weather applications. The Compact Ocean Wind Vector Radiometer (COWVR) represents one of these next-generation MW radiometers, engineered for rapid deployment and cost efficiency, with the objective of delivering ocean surface vector wind (OSVW) data of consistent quality with on-orbit performance comparable to legacy satellites like WindSat (Gaiser et al. 2004). COWVR is a fully polarimetric conical imaging MW radiometer, functioning at frequencies of 18.7 GHz, 23.8 GHz, and 33.9 GHz. Its capabilities encompass the measurement of OSVW, precipitation, and cloud liquid water (CLW). One important feature of COWVR is that it captures data on both the forward (fore) and rear (aft) aspects of each rotation of its conically scanning feed horn, which is essential for accurate retrieval of wind direction (Gaiser et al. 2004).

Several innovative design features have significantly reduced the mass, power consumption, and volume of COWVR. These enhancements include a single multifrequency feed horn, an internal polarimetric calibration source, and a compact monolithic MW integrated circuit (MMIC) receiver. Figure 1a shows the instrument design, featuring a single multifrequency feed horn illuminated by a 360° conical scanning reflector. This reflector rotates at 30 RPM, offering a spatial resolution of better than 35 km and a swath width of approximately 890 km when positioned at the altitude of the International Space Station (ISS). An orthomode transducer splits the signal from the feed into two linear orthogonal components that are then channeled through waveguides to the MMC multifrequency receivers. These receivers serve to amplify and filter the input signals before forwarding them to a hybrid combining polarimetric backend unit. This backend unit is responsible for conducting analog in-phase and quadrature phase cross-correlation of the two signals, yielding the four polarized outputs, including +45, -45, left, and right circular polarization.

COWVR was successfully launched on December 21, 2021, and was installed on the ISS on January 7, 2022 (Fig. 1b). High-quality scientific data has been continuously available since January 8, 2022.

Manuscript approved June 07, 2024.

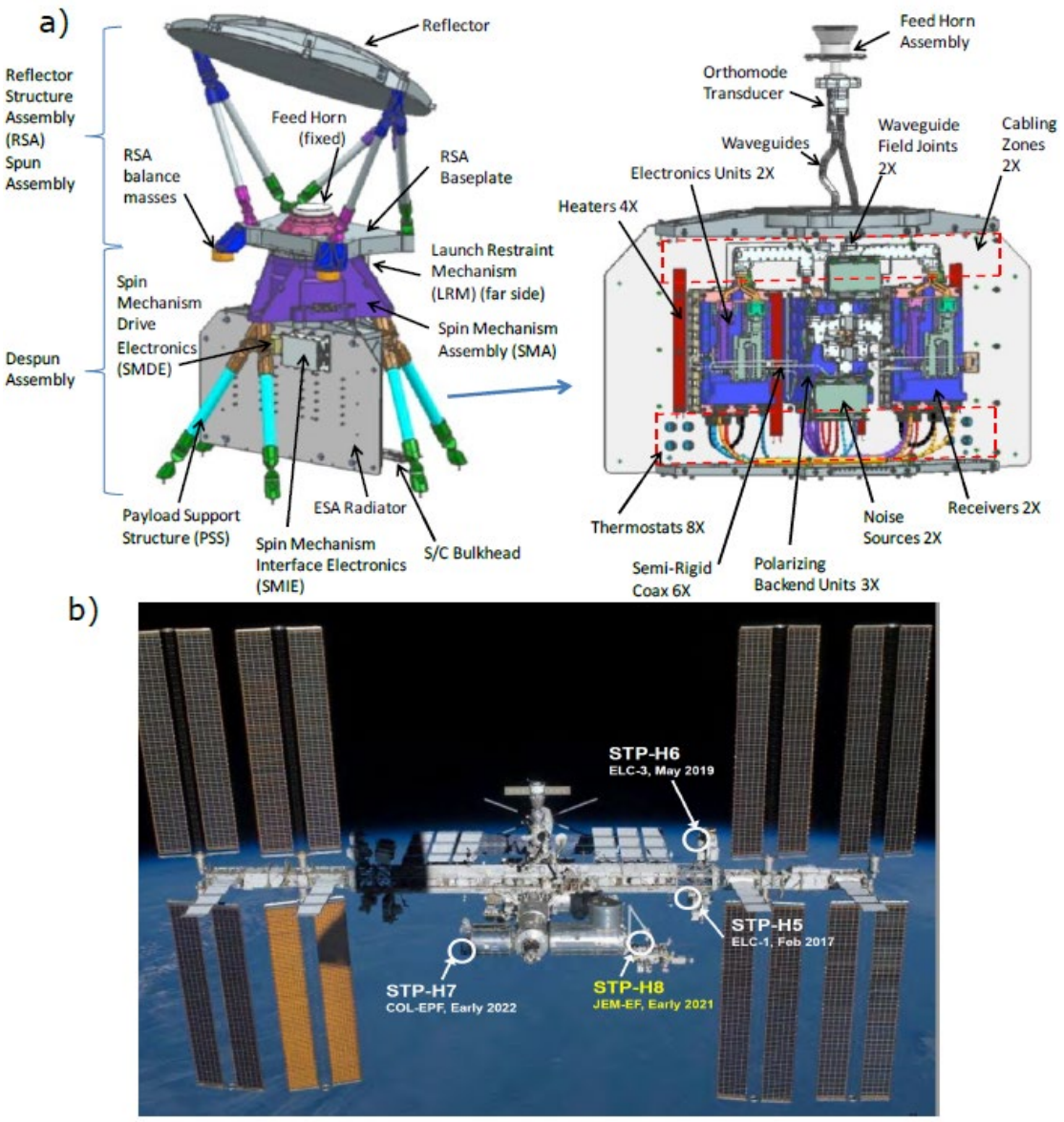

Fig. 1—a) The COWVR instrument design and b) the ISS where COWVR was installed at the Japanese Experiment Module-Exposed Facility (JEM-EF) for STP-H8 (Credit: NASA)

Another instrument designed for the STP-H8 program is the Temporal Experiment for Storms and Tropical Systems (TEMPEST) (Reising et al. 2021). TEMPEST is a cross-track MW radiometer designed to measure total precipitable water (TPW), CLW, and cloud ice. It is primarily a humidity sensor with sounding channels at 165, 176, 180, and 183 GHz, plus an imaging channel at 91 GHz. Both COWVR and TEMPEST aim to deliver high-quality atmospheric observations comparable to those provided by legacy weather satellites but in a much smaller and more cost-effective package. Initially, our investigation will focus solely on COWVR; subsequently, we plan to demonstrate the synergy between COWVR and TEMPEST.

In this study, we provide data and materials in Section 2, discuss our methodology for quality control (QC), bias correction, experimental design, and forecast evaluations in Section 3, and present detailed results concerning the impacts of COWVR in Section 4. We conclude with a summary of the study and our considerations for future directions.

2 DATA AND MATERIALS

2.1 Description of the model and data assimilation system

This study employs NAVGEM, which operates at a horizontal resolution of approximately 31 km (spectral triangular truncation of T425) and includes 60 vertical levels extending up to 0.04 hPa. NAVGEM's spectral model utilizes a semi-Lagrangian semi-implicit dynamic core, complemented by advanced parametrized physics packages (Hogan et al. 2014). The data assimilation (DA) system is the NRL atmospheric variational data assimilation system-accelerated representer (NAVDAS-AR) (Xu et al. 2005, Rosmond and Xu 2006, Kuhl et al. 2013), a dual-space strong-constraint four-dimensional variational (4DVar) hybrid approach. The DA system routinely assimilates a vast array of observations, numbering in the millions, within each 6-h data assimilation window. These observations are derived from a diverse set of sources, including MW and infrared (IR) sensors, conventional platforms (radiosondes, buoys, ship and aircraft data), satellite-derived atmospheric motion vectors (AMVs), Global Navigation Satellite System ground-based receivers, space-borne radio occultations, and trace gas retrievals (Stone et al. 2020, Christophersen et al. 2023).

2.2 COWVR Data and RFI Detection and Mitigation

The COWVR data specification includes the raw data record (RDR), the temperature and sensor data record (TSDR), and the environmental data record (EDR) for various applications. In this study, we focus on the examination of COWVR's geophysical information and radiance data from the EDR. Note that the radiances in the EDR replicate the products from the temperature and sensor data record. The use of EDR data allows us to explore wind retrievals besides radiances. For this study, we concentrated only on the assimilation of radiance data at the composite fields of view (CFOVs). The CFOV measurement is a weighted average of instantaneous field-of-view measurements that is conceptually similar to superobbing, calculated on the ground using a resampling algorithm. Although the fully polarimetric COWVR produces four polarized outputs, our DA system only utilizes the vertical and horizontal polarization components.

The Calibration and Validation (CalVal) team has encountered a series of unprecedented challenges in their mission to accurately geolocate measurements and to eliminate noise, intrusions, and obstructions, some of which stem from COWVR's unique positioning on the ISS. They are also tasked with continuously monitoring sensor measurement trends to diagnose unforeseen anomalies. One crucial aspect of this monitoring is the detection of broadband radio frequency interference (RFI) caused by adjacent channels from geostationary satellites. COWVR's conical scanning at lower MW frequencies provides a distinct advantage by enabling the use of opposing looks at each scene location (both fore and aft) to identify potential geostationary RFIs.

The fundamental detection methodology begins with finding areas over the ocean where significant fore/aft differences have occurred more frequently than expected. If these large differences (outliers) were caused by geostationary sources, they should occur when the COWVR boresight vector was aligned with transmissions from geostationary satellites reflected off the ocean surface. Without knowing in advance the exact location(s) of the relevant geostationary transmitters, we cannot calculate the glint angle between each observation boresight vector and each potential RFI source. We can instead trace the reflection of the

boresight vector for each outlier off the ocean surface up to the geostationary orbit altitude of 35,785 km (hereafter referred to as "reflection endpoint") and look for clusters near the Equator. Figure 2a shows the reflection endpoints for elevated fore-look observations surrounding Hawaii, with a distinct cluster near a geostationary orbit location of 114°W. Similarly, Figure 2b shows the reflection endpoints for elevated aft-look observations along the U.S. Gulf and Atlantic coasts, with a distinct cluster near a geostationary orbit location of 107°W. As shown in Fig 3, there was an increased prevalence of fore-minus-aft outliers near Hawaii and of aft-minus-fore outliers near the U.S. Gulf and Atlantic coasts. We created polygonal boundaries to outline specific areas of the ocean where we have observed RFI outliers. For each of these areas, we defined a square encompassing the location in geostationary orbit where the detected RFI presumably originated. So for the RFI flag to be set, an observation must be in one of the geographic polygons and must have its reflection endpoint lie within the corresponding square.

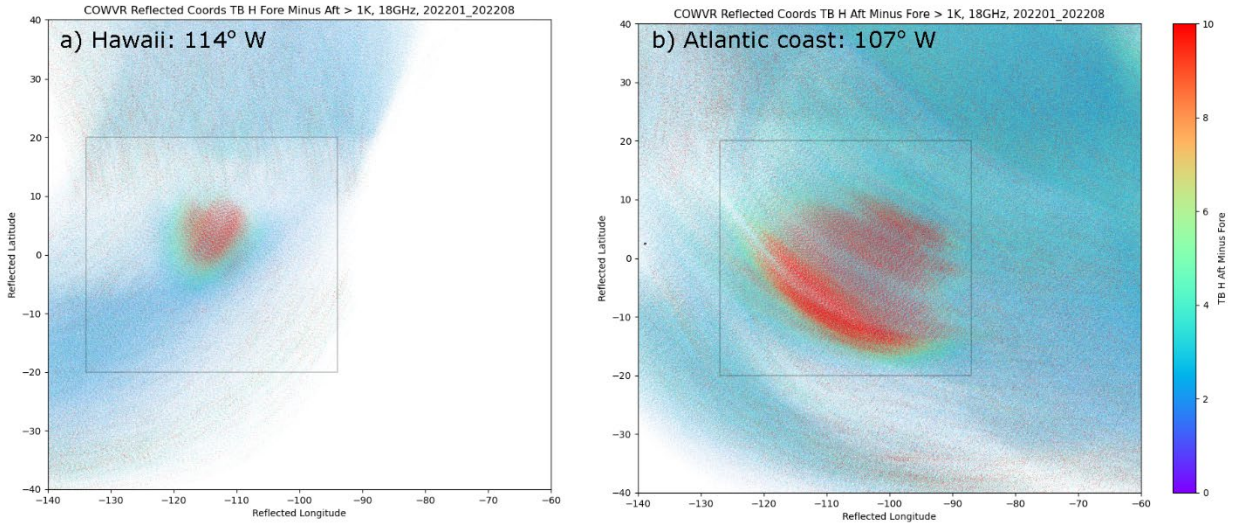

Fig. 2—Latitude and longitude of reflection vectors (boresight or observation vector reflected off the Earth observation ocean surface and traced up to geostationary altitude). The color indicates the fore/aft brightness temperature difference (K) at H-pol 18 GHz. Gray boxes represent the indicated location +/- 20° in both latitude and longitude centered on 114° W and 107° W, respectively, at the Equator. COWVR data from January to August 2022 is used here.

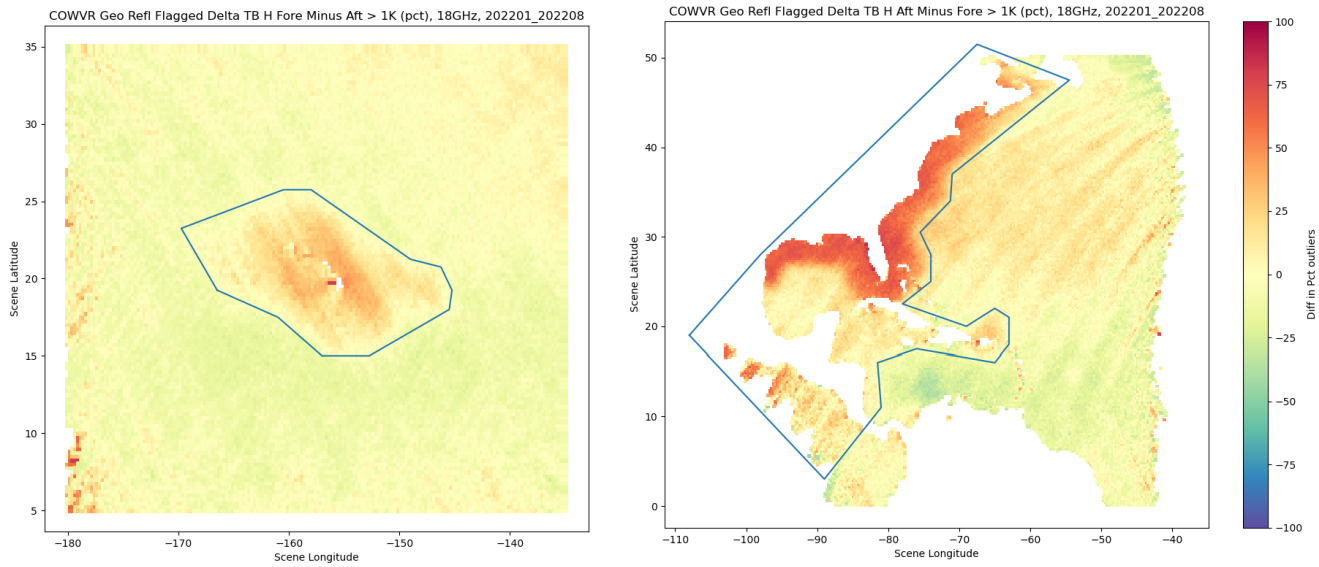

Fig. 3—Corresponding locations of the Earth scenes for Fig. 2 binned by 0.5-degree increments of latitude and longitude. For each bin, observations are split into two groups, where one group has a reflection endpoint inside the square region in Fig. 2 and the other group has reflection endpoints outside the square region. The percentage of observation with fore/aft delta (fore minus aft) greater than 1 K for H-pol 18 GHz within each group is calculated. The percentage difference is indicated by the colorbar. The polygon is drawn subjectively around locations that show large percentage differences (mostly positively differences).

Since the initial development of the RFI flag using the above "polygon-and-square" approach, an improved method is under development to create a lookup table to characterize the strength of geostationary RFI observed over 12 months for all four 18-GHz channels at four-dimensional coordinates: scene longitude, scene latitude, reflection endpoint longitude, and reflection endpoint latitude. This not only allows the identification of areas where known RFI occurs (i.e., observed 18-GHz H-pol RFI exceeds some threshold), but also offers a correction value. This correction can potentially mitigate the impact of known RFI on all 18-GHz channels.

3 METHODOLOGY

3.1 COWVR Quality Control

Due to the exceptional challenges associated with mounting COWVR on the ISS, COWVR has undergone extensive CalVal testing, resulting in numerous iterations of data versions to accommodate unforeseen changes. For the current study, we employed COWVR EDR data from version 752, augmenting with various flags for factors like solar array intrusion, support arm status, RFI, rain detection, and observation quality. Additional QC procedures for the COWVR data involve the following steps:

1. A gross error check is performed on the physical values of the observations within the assimilation window.
2. Observations with brightness temperature (BT) differences between 18 GHz and 34 GHz exceeding 15 K are filtered out. This step aims to identify possible RFI that might not have been detected by the RFI flag. (Note: this filtering is no longer needed for COWVR data beyond version 800.)

3. A cloudy scene check is performed using an empirical regression (Eq. (1)) to estimate CLW from BTs at 18, 23, and 34 GHz, along with their polarization components (V and H):

$$CLW = max\{0 \mid c_1 + c_2 T_{18V} + c_3 T_{18H} + c_4 T_{23V} + c_5 T_{23H} + c_6 T_{34V} + c_7 T_{34H} + c_8 T_{34H}{}^2\}. \quad (1)$$

   The sets of coefficients c_i differ as a function of Earth incidence angle for COWVR, from 48 to 59 degrees (Table 1). The CLW regression is similar to the regression used for the legacy SSMI/S instrument to retrieve TPW and CLW (Alishouse et al. 1990a, Alishouse et al. 1990b, Zheng et al. 2014). A conservative threshold of 0.18 mm is used to identify scenes potentially contaminated by clouds or rain, which is a more stringent filter than the rain flag in the EDR dataset.

4. The final QC step involves a radiance innovation (observed minus background) check, where observations are filtered out if their innovation magnitude is three times larger than the square root of the sum of the observation error and the background error variance.

The CFOV radiances are further thinned at 1.75° latitude-and-longitude boxes, and temporally at 30 minutes to match the DA time integration in the solver. Within each thinning box, two observations, one fore and one aft, are kept for assimilation. COWVR radiances over ocean only are evaluated in this study.

Table 1—Coefficients for Eq. (1) to Empirically Derive CLW

	Earth incident angle (degree)											
	48	49	50	51	52	53	54	55	56	57	58	59
c_1	2.7E+00	2.7E+00	2.7E+00	2.7E+00	2.7E+00	2.7E+00	2.7E+00	2.7E+00	2.6E+00	2.6E+00	2.6E+00	2.7E+00
c_2	5.4E-03	6.3E-03	7.2E-03	8.2E-03	9.3E-03	1.0E-02	1.1E-02	1.2E-02	1.3E-02	1.3E-02	1.4E-02	5.4E-03
c_3	-1.4E-02	-1.5E-02	-1.6E-02	-1.7E-02	-1.8E-02	-1.8E-02	-1.9E-02	-2.0E-02	-2.1E-02	-2.1E-02	-2.2E-02	-1.4E-02
c_4	-9.0E-03	-8.6E-03	-7.9E-03	-7.5E-03	-7.1E-03	-6.7E-03	-6.4E-03	-6.1E-03	-5.9E-03	-5.7E-03	-5.5E-03	-9.0E-03
c_5	-2.9E-02	-2.9E-02	-3.0E-02	-3.0E-02	-3.0E-02	-3.0E-02	-3.0E-02	-3.0E-02	-3.0E-02	-3.0E-02	-2.9E-02	-2.9E-02
c_6	1.6E-02	1.6E-02	1.6E-02	1.7E-02	1.7E-02	1.7E-02	1.7E-02	1.7E-02	1.7E-02	1.7E-02	1.7E-02	1.6E-02
c_7	2.5E-03	2.1E-03	1.6E-03	1.1E-03	8.0E-04	3.1E-04	-4.1E-05	-3.2E-04	-6.3E-04	-9.4E-04	-1.3E-03	2.5E-03
c_8	7.9E-05	7.8E-05	7.7E-05	7.7E-05	7.6E-05	7.5E-05	7.4E-05	7.3E-05	7.2E-05	7.1E-05	7.0E-05	7.9E-05

3.2 Variational Bias Correction

Variational bias correction (VarBC) is a commonly used approach to identify and rectify systematic biases that may arise from instrument calibration, ground data processing, forward operator, and/or model related biases (Derber and Wu 1998, Dee 2004, Dee and Uppala 2009, Zhu et al. 2014), and error of representation. Typically, the bias is broken into two main components: an air-mass component (b^{air}) and a satellite angle component (b^{angle}). The bias-corrected observation (forward) operator $\tilde{h}$ for a specific channel of a satellite sensor connects model state $\boldsymbol{x}$ to the observed data at a particular time and location by

$$\tilde{h}(\boldsymbol{x}, \beta) = h(\boldsymbol{x}) + b^{air}(\boldsymbol{x}, \beta) + b^{angle}, \tag{2}$$

where $h(\boldsymbol{x})$ denotes the uncorrected observation operator (i.e., the radiative transfer model plus horizontal interpolation). The air-mass-dependent bias b^{air} can be expressed as a linear regression,

$$b^{air}(\boldsymbol{x}, \beta) = \beta_0 p_0 + \sum_{i=1}^{N} \beta_i p_i(\boldsymbol{x}), \tag{3}$$

with scalar predictor coefficients $\beta_i, i = 0, \ldots N$ and atmospheric state-dependent vector predictors $p_i(\boldsymbol{x})$. All predictors except the constant are standardized (i.e. shifted and scaled to have zero mean and unit variance, nondimensional), and all of the coefficients have units matching the observation (here BT in K). The three predictors $p_i(\boldsymbol{x}), i = 0,1,2$ in NAVGEM are a global offset ($p_0 = 1$) and the atmospheric layer thicknesses from 300 hPa to 850 hPa (p_1) and from 50 hPa to 200hPa (p_2). The satellite-angle-dependent bias b^{angle} is typically given by a polynomial regression of satellite angle (e.g., scan angle, zenith angle). Initially, given that COWVR is conical scanning radiometer, the VarBC scheme applied to COWVR did not include the satellite angle-dependent component; however, further analysis revealed that the mean innovation is indeed dependent on satellite scan angles, as detailed in the results presented in Section 4.1. Additionally, the mean innovations for fore and aft scenes exhibited different dependencies on satellite angles. To address this, a binary indicator is introduced to differentiate fourth-order-polynomial fits for fore and aft scenes for each channel,

$$b^{angle} = \mathrm{j} \sum_{i=0}^{4} \alpha_i \varphi^i + (1 - j) \sum_{i=0}^{4} \gamma_i \varphi^i, \tag{4}$$

where j is a binary variable (0 or 1) indicating whether the scene corresponds to a fore or aft look. The angle (φ) has been tested using the spacecraft scan angle (a combination of the instrument scan angle and the spacecraft yaw) as well as the instrument scan angle. Bias correction coefficients α and γ are updated online at each DA cycle as part of VarBC. Further details and results will be presented in Section 4.1.

3.3 Experiment Design

We conducted a set of experiments, the first part of which tests VarBC with various predictors for COWVR bias (as detailed in Section 3.2). The second part compares experiments with and without the assimilation of COWVR radiances (Table 2). Note that the current NAVDAS-AR system assimilates clear-sky radiances only. Because COWVR's channels closely resemble those of existing MW sensors like the Defense Meteorological Satellite Program (DMSP) Special Sensor Microwave Imager/Sounder (SSMI/S) and the Advanced Technology Microwave Sounder (ATMS), the observation error variances associated with the COWVR channels in the COWVR impact experiments are assigned to be the same as those for the corresponding SSMIS and ATMS channels. In contrast, the VarBC experiments utilize a mean of Desroziers-diagnosed errors and errors from existing MW sensors like SSMIS and ATMS (Campbell et al. 2017).

Our experiments were conducted in 2022 from August 15, 0000 UTC to October 1, 0000 UTC. The operational NAVGEM satellite bias coefficients and restart files valid at 0000 UTC on August 15, 2022, were employed as initial conditions. The COWVR bias coefficients were initialized to zero for all predictors.

Table 2—Description and Specifications of the Experiments

	Experiment name	Assimilated Observations	COWVR	
			Number of VarBC Predictors	Observation Error Standard Deviation (K)
VarBC set	exp_3preds	Baseline plus COWVR	3	3.5–3.8 for V, 4.4-5.1 for H
	exp_13preds	Baseline plus COWVR	13	3.5–3.8 for V, 4.4–5.1 for H
COWVR Impact set	cntl	Baseline	/	/
	exp_cowvr	Baseline plus COWVR	13	4.5 for V, 5.5 for H

"Baseline observations" refers to the dataset routinely assimilated by the operational NAVGEM as of August 2022.

3.4 Forecast Evaluation

We assess the quality of forecasts by comparing a control run with an experimental run against various benchmarks, including self-analysis, independent analyses from different operational centers, and a set of high-quality radiosondes. Relative impact is calculated using the following formula:

$$\text{relative impact} = 100 * (RMSE_{cntl} - RMSE_{exp})/RMSE_{cntl}, \quad (5)$$

where the root mean square error (RMSE) is computed for forecast fields such as geopotential height, wind, temperature, and moisture at regular latitudinal-longitudinal grids at 0.5° resolution. These RMSE values are compared against a reference dataset at 12-h intervals on a global scale or within specific regions (e.g., the Northern Hemisphere (NH; 20°–80°N), the Tropics (TR; 20°S–20°N), and the Southern Hemisphere (SH; 20°–80°S)). The statistical confidence in the performance difference between the control and experimental runs can also be quantified, as discussed by Christophersen et al. (2023) and Kuhl et al. (2013).

Additionally, we use forecast sensitivity to observation impact (FSOI) (Langland and Baker 2004) to evaluate the impact of COWVR on short-range forecasts (24 h and 30 h) in the experimental run where COWVR radiances are assimilated. FSOI uses the total moist energy error norm as described by Baker et al. (2022).

Furthermore, we perform a 6-h forecast comparison against observations, commonly known as "fit to observations" (Bauer et al. 2011, Geer 2019, Geer et al. 2010, Frolov et al. 2020), to examine the impact of COWVR assimilation on other observations incorporated into the system. This evaluation helps determine whether COWVR assimilation enhances or impairs the performance of observations in specific atmospheric vertical regimes, inferred from the characteristics of channels (e.g., sensitivity to low- or midlevel water vapor, temperature).

4 RESULTS

4.1 COWVR VarBC Scheme

Given that COWVR is a conical imaging radiometer, the initial bias-correction scheme implemented only the constant and two air-mass dependent bias correction components. This three-predictor VarBC scheme was able to remove large systematic biases for all three frequencies; however, Fig. 4a shows a clear residual scan angle dependence in all three COWVR channels, most prominently in the 23-GHz channel. Spacecraft scan angle predictors are traditionally used in the VarBC scheme for legacy MW sensors like SSMIS and ATMS. Figure 4a shows that the fore scenes were divided into halves when fitted with standard polynomial functions in the range of [0, 360] for spacecraft scan angle. Given the obstructed views (hence some data gaps in the continuous 360° rotation, Fig. 4) in between fore and aft looks, this suggests that one polynomial function with respect to spacecraft scan angle to correct scan angle dependence might not be sufficient. The enhanced VarBC scheme in "exp_13preds" incorporates instrument scan angles and derives respective predictor coefficients for fore and aft scenes and significantly mitigates the scan angle dependence (Fig. 4b).

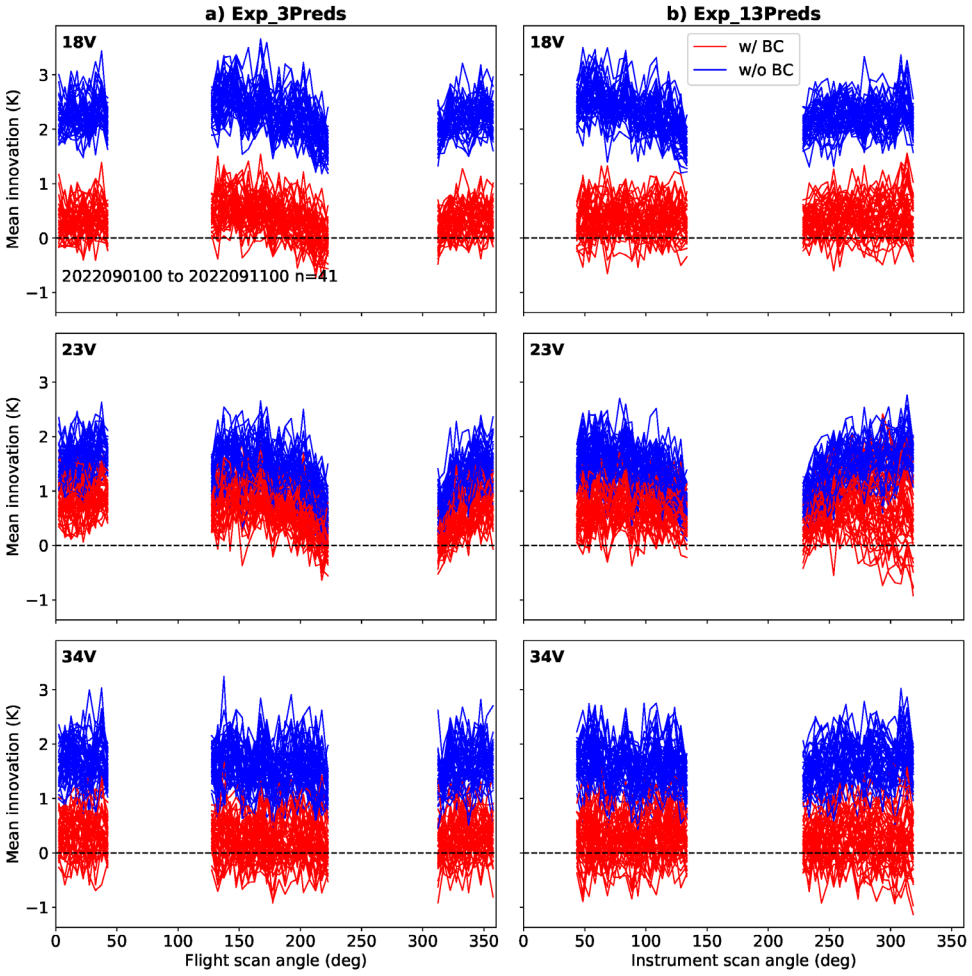

Fig. 4—Mean innovations for the vertical polarization of 18, 23 and 34 GHz as a function of (a) ISS flight scan angle from the "exp_3preds" and (b) COWVR instrument scan angle from the "exp_13preds" during September 1–10, 2022. Each line represents the mean innovation for a given 6-h data assimilation cycle.

Figure 5 presents the time series of predictor coefficients for the "exp_13preds." The first three predictor coefficients behave similarly to those in the "exp_3preds." Most of the coefficients seem to stabilize after approximately 10 days of cycling. The coefficients up to the second-order polynomial fit for the fore scenes exhibit similar temporal variations to those of the aft scenes.

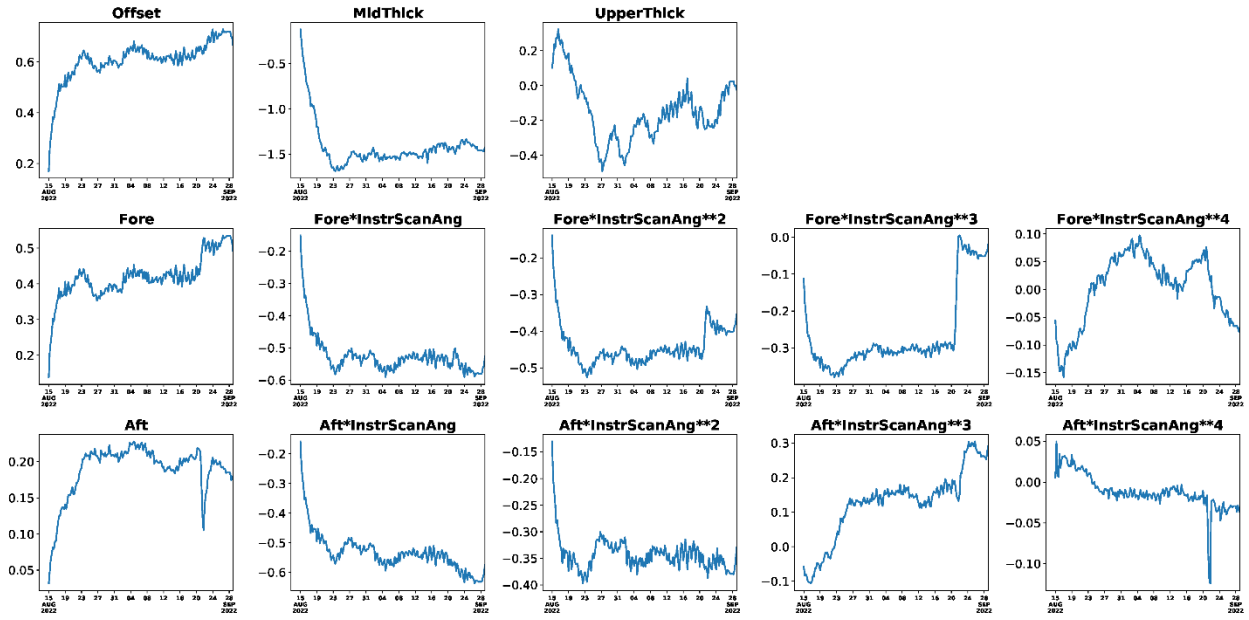

Fig. 5—Time series of various predictor coefficients for COWVR channel 1 (V-pol 18.7 GHz) for the experiment with 13 predictors ("exp_13preds") from August 15, 2022, to September 30, 2022. Each predictor is explained in the text. The time series of the three predictor coefficients for the "exp_3preds" experiment is similar to those shown in the first row.

The transition from three predictors to 13 predictors in the VarBC schemes results in minor changes in the global mean innovations, primarily noticeable during the spin-up period (Fig. 6). The mean innovations for the "exp_13preds" exhibit a slightly higher rate of convergence to stability over time. This corresponds to a slight decrease in the mean innovation bias (0.40 K) for "exp_13preds" during the first month of cycling compared to "exp_3preds" (0.45 K). The mean innovations seem to cycle stably after ~10 days for both experiments. Given the improved performance with the instrument scan angle as predictors, most notable in that the residuals are more independent of the instrument scan angle, the remaining COWVR impact experiments will be conducted using this enhanced VarBC scheme.

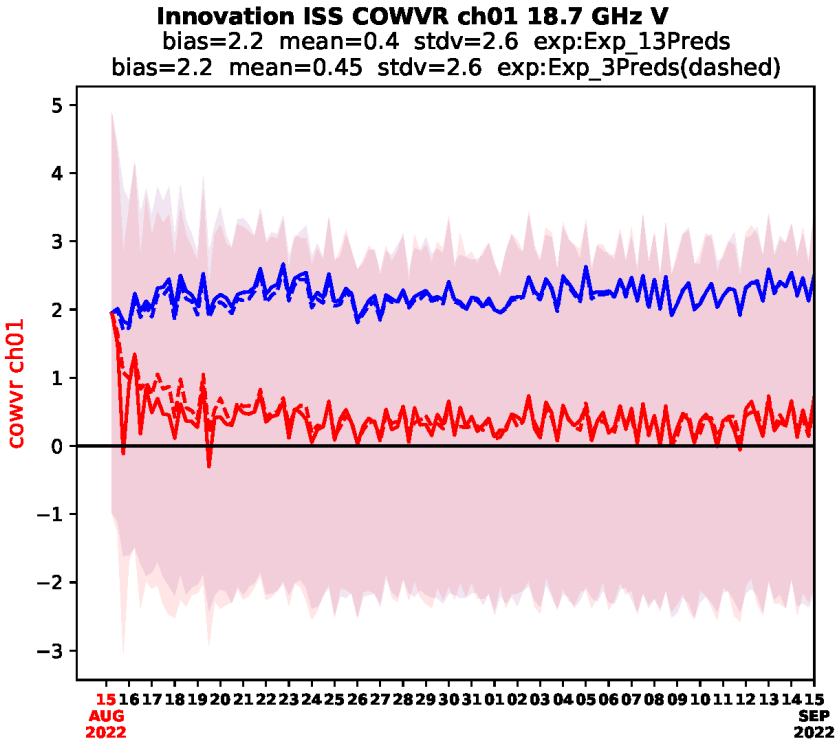

Fig. 6—Time series of global mean innovation (blue/red lines are the raw/bias-corrected mean innovations, respectively) and its standard deviation (light/dark pink shading for the "exp_3preds"/"exp_13preds" experiments, respectively) from August 15, 2022, to September 15, 2022. Innovations beyond September 15 show little variation between the two experiments, similar to the statistics in early September, and hence are not plotted for the sake of simplicity.

4.2 COWVR Impact on Analysis and Forecast

COWVR clear-sky radiances over ocean are integrated into the NAVDAS-AR global DA system along with all other operational observations utilized as of August 2022. The screening for cloud and rain is described in Section 3.1 as a component of the QC.

For September 2022, the most influential sensors within the DA system are the cross-track MW sensors, including ATMS, AMSU-A, and SSMIS (Fig. 7). The COWVR assimilation contributes 12.2% of the reduction in the 24-h forecast error norm, which surpasses the individual contributions from SSMIS DMSP F16 (8.5%), F17 (9.5%), and F18 (7.8%). Note that only 2–3 channels from AMSR-2 and GMI are assimilated (Frolov et al. 2020), which may account for the relatively low FSOI reduction from these sensors. Generally, COWVR exhibits a similar impact to legacy sensors like AMSU-A and SSMIS (Fig. 7).

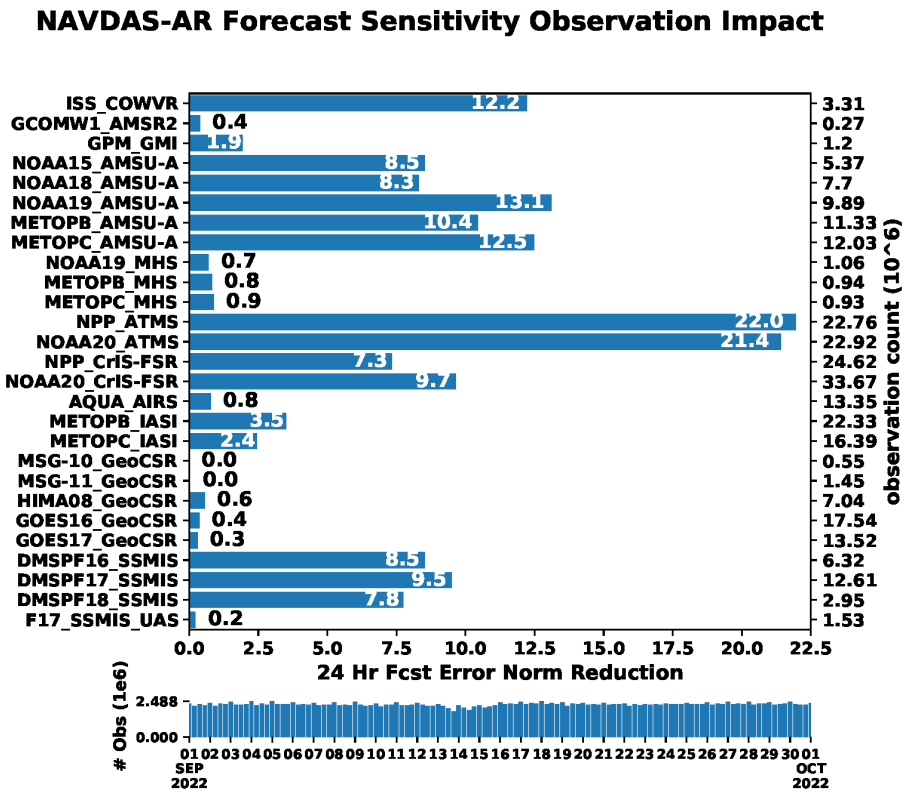

Fig. 7—Percentage of the 24-h total forecast error norm reduction (J/kg, larger is better) by all radiances assimilated in the NAVDAS-AR for September 2022. COWVR radiances are labeled as "ISS_COWVR."

FSOI can also be normalized by total observations and applied at the individual channel level. The per observation FSOI for COWVR at the 18-, 23-, and 34-GHz frequencies is similar to that of SSMIS channels 12–16, which are the most influential channels of SSMIS (Fig. 8b). This suggests that the higher total FSOI for COWVR (Fig. 7) is likely attributed to a higher data count for COWVR than for SSMIS at channels 12-16. Figure 8 (c-d) confirms that total FSOI for COWVR is consistently higher than individual SSMIS at channels 12-16 at each cycling hour as a result of higher data count for COWVR. It is worth noting that COWVR data is thinned at a 1.75° thinning box while SSMIS data is thinned at a 1.25° thinning box. The retention of both fore and aft scenes at a given thinning box might compensate for the coarse thinning for COWVR, resulting in a higher total FSOI. Note that the total data count for individual SSMIS aboard DMSP F16 and F17 is higher than that of COWVR (Fig. 7).

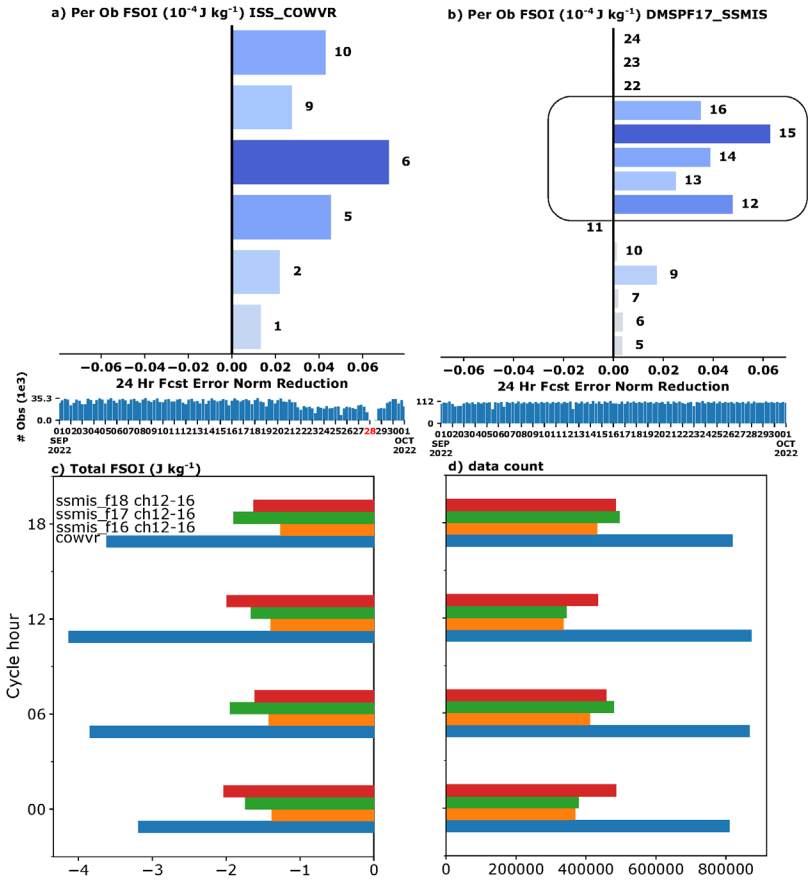

Fig. 8—Per observation FSOI (10^{-4} J/kg) for (a) COWVR and (b) SSMIS aboard DMSP F17 for September 2022. The gray box on the right denotes channels from SSMIS at similar frequencies to COWVR. (c-d) Total FSOI (J/kg) and corresponding data count for COWVR and SSMIS at channels 12-16 for September 2022.

When assessing forecasts against ECMWF analyses, COWVR demonstrates notable positive impacts of 0.5–1.25% on the TR and SH vector wind forecasts at a lead time of 72 h and beyond (Fig. 9). The larger impact for the wind at medium-range lead times may be closely related to the reduction of the small initial wind errors following the COWVR assimilation (Fig. 10). This impact over time is particularly evident in the SH (72h, 96 h and 120 h in Fig. 10). The overall impact over the NH region is neutral on average (Fig. 9).

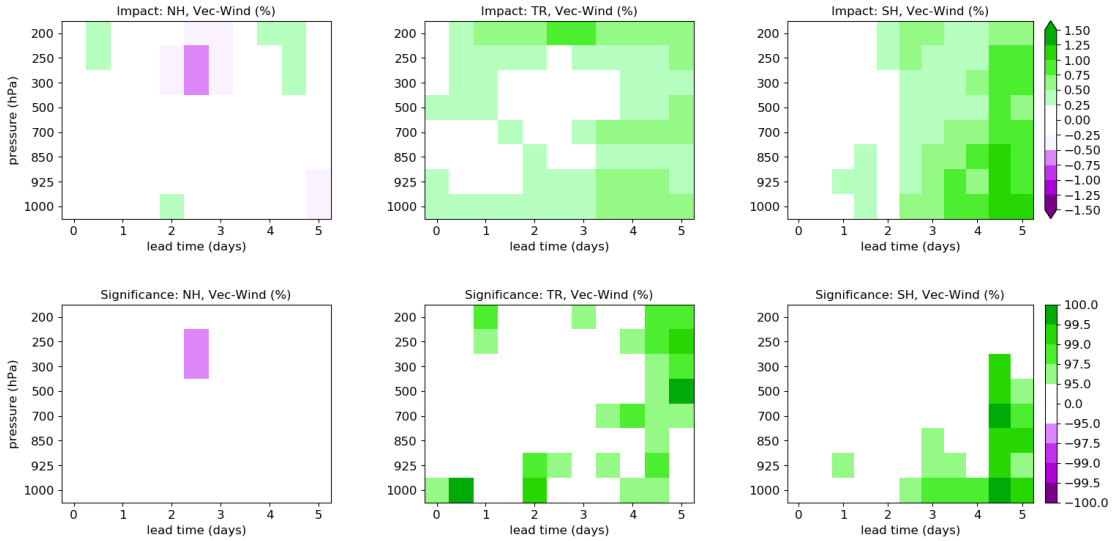

Fig. 9—Relative impact (top row) and associated significance of the impact (bottom row) for 5-day wind forecasts from the COWVR assimilation experiment versus the control (no COWVR), verified against the ECMWF analyses for the NH (20°–80°N), the TR (20°S–20°N), and the SH (20°–80°S) for September 2022. Green indicates improvement, while purple indicates degradation.

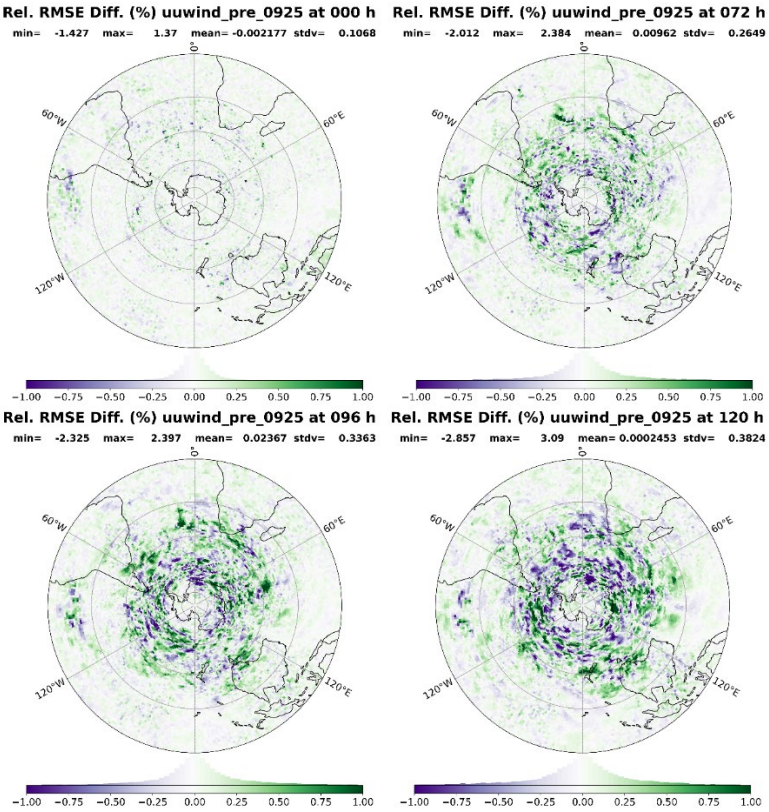

Fig. 10—Average relative impact during September 2022 for zonal wind speed (u-wind) at 925 hPa from the equator to the South Pole verified against ECMWF analyses at forecast lead time 0, 72, 96, and 120 h. Latitudes are labeled at every 20 degrees. Green/purple are improvement/degradation, respectively, due to COWVR assimilation.

Furthermore, COWVR assimilation results in significant positive 0.25–0.75% improvement on low-level precipitable water forecasts over the NH region up to the 72 h of lead time, and about 0.25–1.25% over the TR region up to lead time 96 h (Fig. 11). However, it degrades the low-level precipitable water in the SH by 1–1.5% at the analysis time and adversely affects the low-level temperature forecasts in the SH by 0.5–1% within the first 12 h (Fig. 12). Furthermore, a positive impact of 0.5–1.5% on upper-level temperature forecasts in the SH is seen beyond 96 h (Fig. 12).

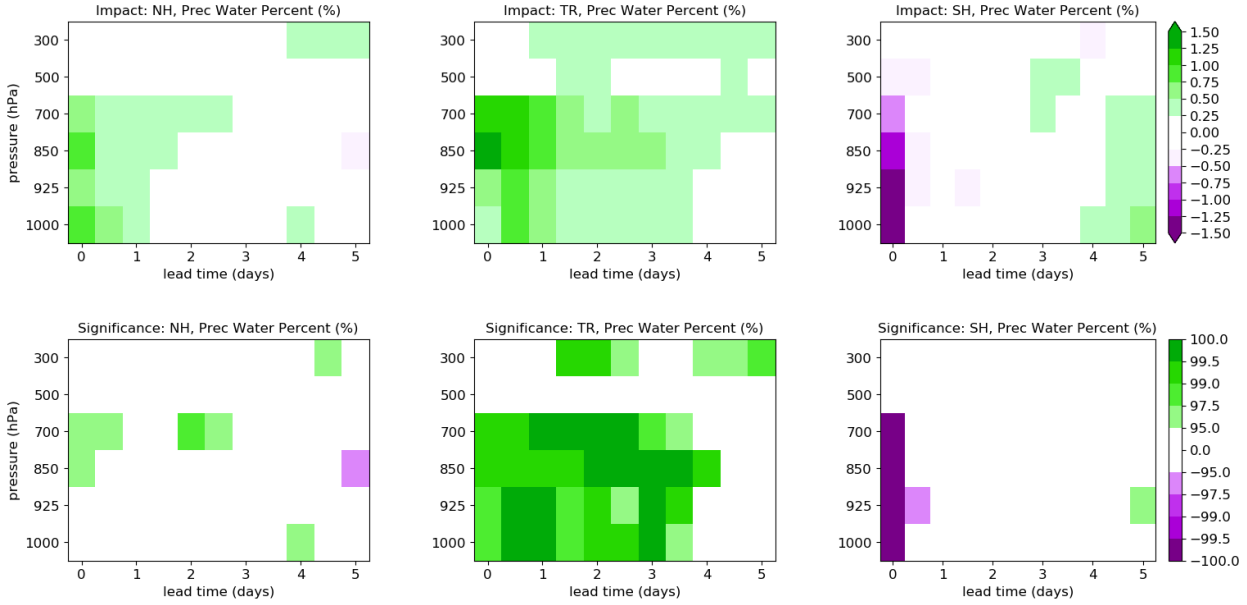

Fig. 11—Same as Fig. 9 but for precipitable water percentage

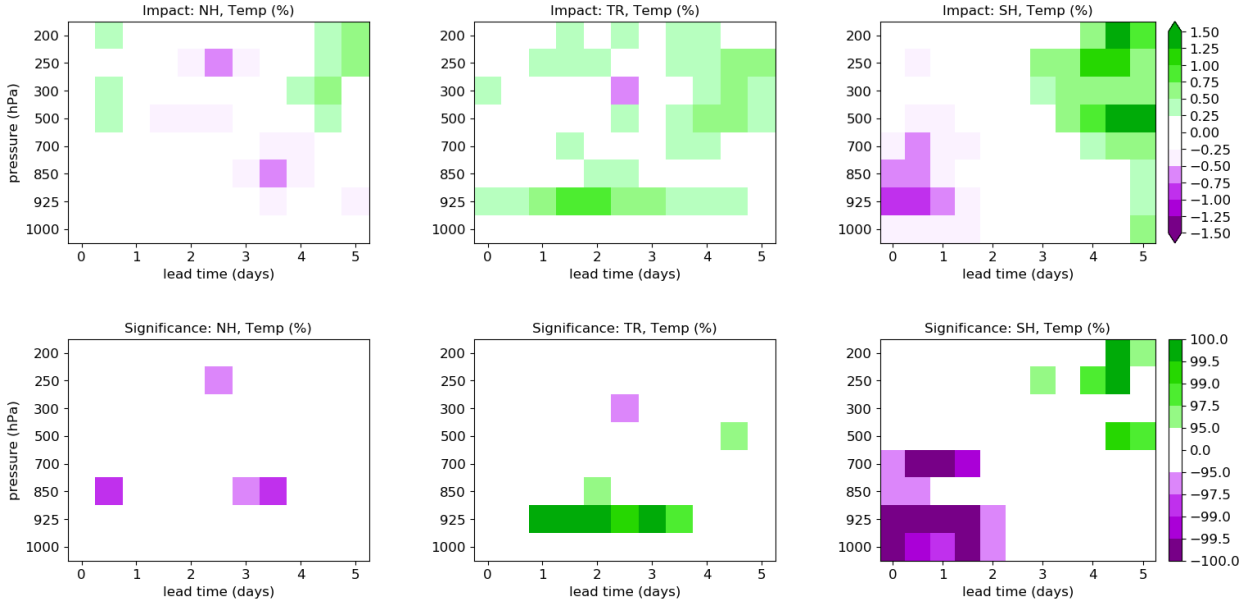

Fig. 12— Same as Fig. 9 but for air temperature

It is worth noting that the assimilation of COWVR radiances impacts wind forecasts more than temperature and moisture forecasts (as evident in Figs. 9, 11, and 12), particularly in the SH. This could be attributed to that the responses in wind forecasts at later lead times are more sensitive to the changes in initial conditions following COWVR radiance assimilation (Fig. 10 versus Fig. 13). Given that COWVR's primary purpose is to derive ocean surface wind vector, it is not surprising that the assimilation of COWVR radiances has a more pronounced impact on wind forecasts compared to other geophysical parameters (Le Marshall et al. 2007).

The slight degradation observed in temperature at the analysis time is noticeable in the 30°–60° S (Fig. 12), and it aligns with the mean innovations in temperature-sensitive channels from sensors like ATMS (Fig. 14). Similarly, the degradation in precipitable water at the analysis time (Fig. 11) is consistent with the degradations seen in the mean innovations for ATMS and SSMIS water vapor-sensitive channels (Figs. 14 and 15).

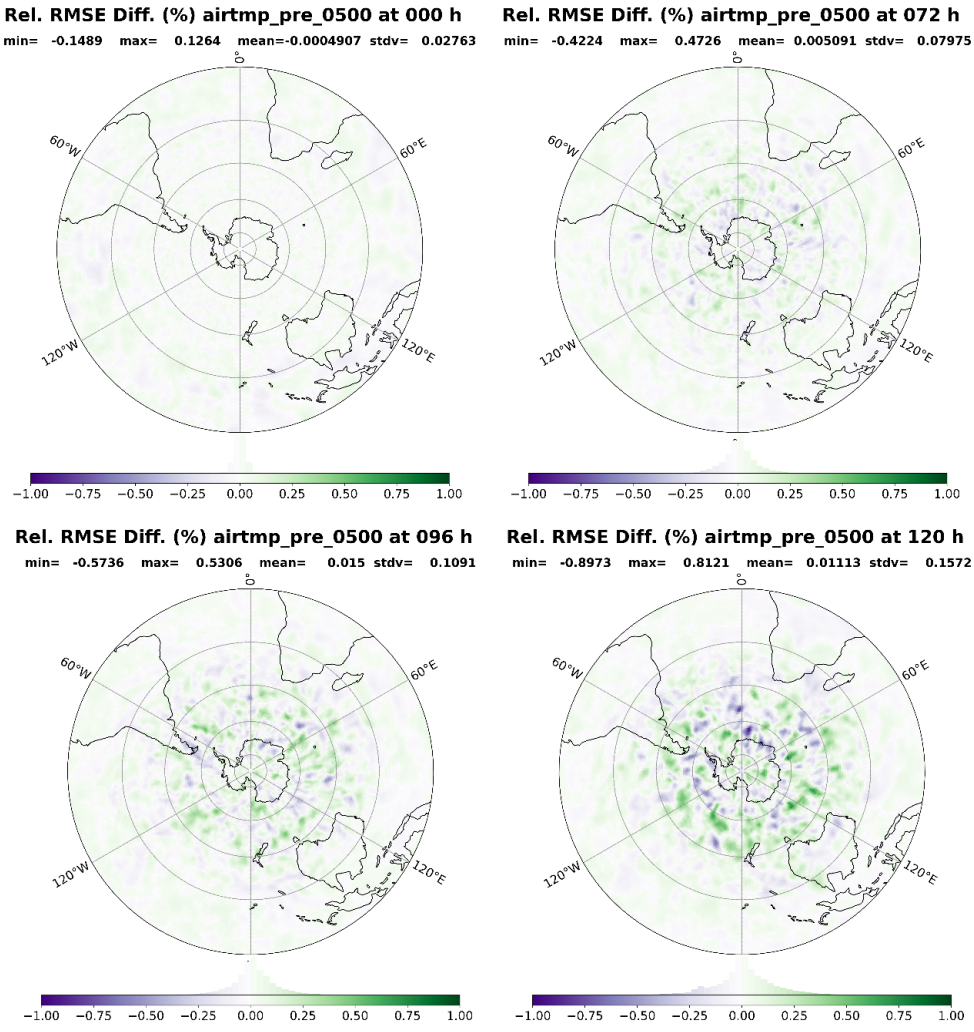

Fig. 13—Same as Fig. 10 but for air temperature at 500 hPa

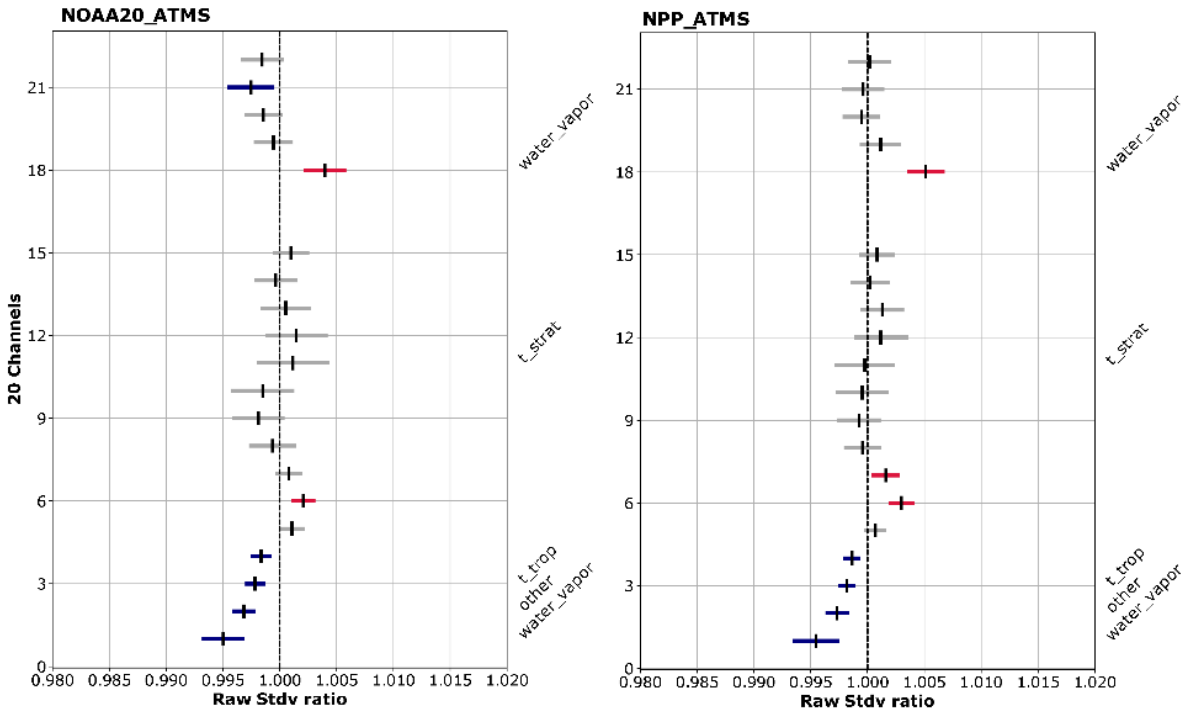

Fig. 14—Ratio of the mean raw standard deviations (aka "fit to observations") of ATMS innovations aboard (left) NOAA and (right) NPP between COWVR experiment ("exp_cowvr") and the control run ("ctl") for September 2022. The horizontal bar denotes the 95% confidence interval (CI) around the mean (black notch). Channels with blue CIs indicate improvement, while those with red CIs suggest degradation, in "exp_cowvr" compared to the control experiment ("ctl"). Gray CIs denote no statistically significant difference.

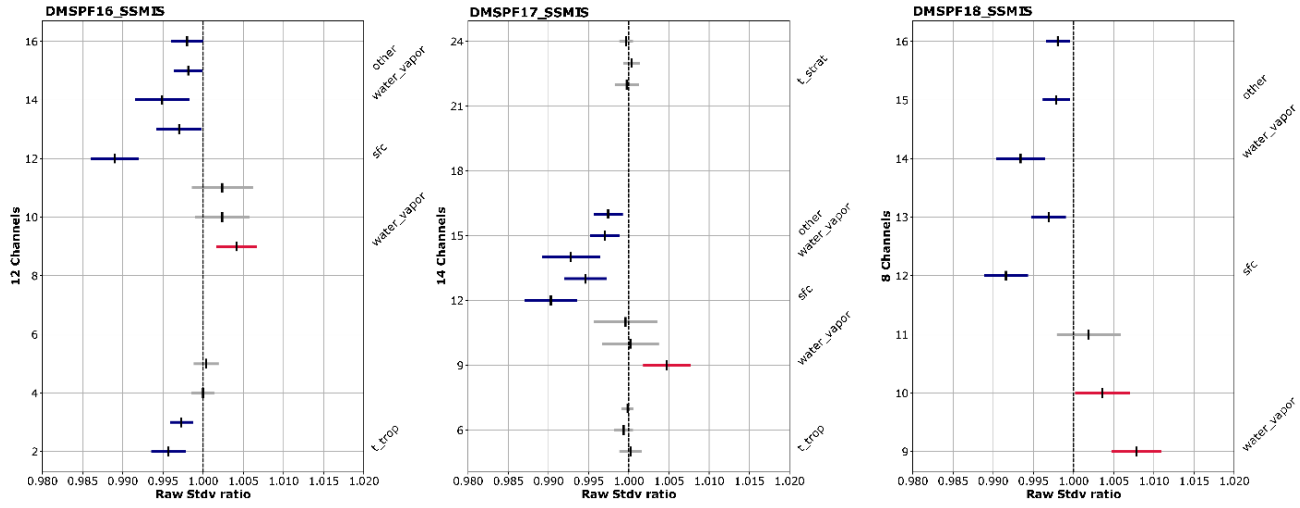

Fig. 15—Same as Fig. 14 but for SSMIS sensors aboard DMSP F16, F17, and F18, respectively

5 SUMMARY AND FUTURE WORK

This study explores the capabilities of a new generation of cost-effective and versatile small satellites like COWVR to determine whether they can provide high-impact Earth observations comparable to traditional weather satellites. We evaluated the impact of COWVR radiances using the NAVGEM (Hogan et al. 2014) and its DA system NAVDAS-AR (Xu et al. 2005, Rosmond and Xu 2006, Kuhl et al. 2013). We used various metrics, including FSOI (Langland and Baker 2004), and scorecards for geophysical fields at different regions and pressure levels with different reference data sources. Our findings indicate that clear-sky ocean-only COWVR radiances can have a comparable positive impact on 24-h model forecasts as the radiances from legacy MW sensors. COWVR radiances exhibit a more pronounced impact on wind forecasts beyond the 48-h lead time compared to temperature and moisture forecasts. Some degradations in short-range low-level temperature and moisture forecasts are observed, aligning with the performance of temperature and moisture-sensitive channels from other legacy sensors like ATMS and SSMIS.

We are actively exploring the performance of SmallSats sensors, especially with regard to potential spatial and temporal uncertainty variability inherent to these small satellites. Initial diagnostics using Desroziers estimates (Desroziers et al. 2005) also suggest that observation uncertainty, even for legacy sensors, may vary by season or region. Furthermore, there is potential for improving the variational bias scheme implemented for COWVR angle correction by investigating potential collinearity issues arising from the constant parameter indicating fore or aft looks. Additionally, with the presence of both COWVR and TEMPEST on ISS, where TEMPEST can provide rich moisture information, combining these two datasets may lead to synergies in characterizing environmental conditions that could further enhance forecasts. The derived ocean surface wind vector products can also be assimilated into NWP models, as we routinely do in the current DA system (Stone et al. 2020, Christophersen et al. 2023).

In summary, our study highlights the significant potential of technology demonstration instruments such as COWVR for numerical weather prediction. The source codes from this study have been delivered to the Fleet Numerical Meteorology and Oceanography Center (FNMOC), indicating the imminent routine assimilation of COWVR data into the operational DA system.

ACKNOWLEDGMENTS

The authors acknowledge funding support from the U.S. Naval Research Laboratory (NRL) base project number (N0001423WX00011) and computing resources provided by the NRL local clusters. The U.S. Space Force (USSF) Space Systems Command (SSC) is a sponsor for this work. The authors declare no conflicts of interest.

DATA AVAILABILITY STATEMENT

The NAVGEM forecasts as well as satellite data are stored at the NRL local clusters and are controlled unclassified data that require users to register with the U.S. government and to acquire permission prior to use. More details can be found online (https://www.nrlmry. navy.mil/metoc/nogaps).

REFERENCES

1. Alishouse, J. C., J. B. Snider., E. R. Westwater, C. T. Swift, C. S. Ruf, S. A. Snyder, J. Vongsathorn, and R. R. Ferraro, 1990a: Determination of Cloud Liquid Water Content Using the SSM/I. IEEE Transactions on Geoscience and Remote Sensing, 28, 817–822.
2. Alishouse, J. C., S. A. Snyder., J. Vongsathorn, and R. R. Ferraro, 1990b: Determination of oceanic total precipitable water from the SSM/I, IEEE Transactions on Geoscience and Remote Sensing, 28, 811-816.

3. Baker, N. L., Pauley, P. M., Stone, R. E., and Langland, R. H. (2022). Interpretation of forecast sensitivity observation impact in data denial experiments. In Data assimilation for atmospheric, oceanic and hydrologic applications (Vol. IV). Springer International Publishing. https://doi. org/10.1007/978-3-030-77722-7.

4. Bauer, P., R. Buizza, C. Cardinali, and J. Thepaut, 2011: Impact of singular-vector-based satellite data thinning on NWP. Quarterly Journal of the Royal Meteorological Society, 137, 286-302.

5. Campbell, W. F., E. A. Satterfield, B. Ruston, and N. L. Baker, 2017: Accounting for correlated observation error in a dual-formulation 4D variational data assimilation system. Monthly Weather Review, 145, 1019-1032.

6. Christophersen, H., B. Ruston, and N. L. Baker, 2023: Assimilation of GNSS Zenith Total Delay in NAVGEM Journal of Geophysical Research: Atmospheres. Journal of Geophysical Research Atmospheres, 1-17.

7. Dee, D. P., 2004: Variational bias correction of radiance data in the ECMWF system. Proceedings of workshop on assimilation of high spectral resolution sounders in NWP, Reading, UK.

8. Dee, D. P., and S. Uppala, 2009: Variational bias correction of satellite radiance data in the ERA-Interim reanalysis. Quart. J. Roy. Meteor. Soc., 135, 1830–1841.

9. Derber, J. C., and W. Wu, 1998: The use of TOVS cloud-cleared radiances in the NCEP SSI analysis system. Quarterly Journal of the Royal Meteorological Society, 126, 2287-2299.

10. Desroziers, G., L. Berre, B. Chapnik, and P. Poli, 2005: Diagnosis of observation, background and analysis-error statistics in observation space. Quarterly Journal of the Royal Meteorological Society, 131, 3385-3396.

11. Frolov, S., W. F. Campbell, B. Ruston, C. H. Bishop, D. Kuhl, M. Flatau, and J. McLay, 2020: Assimilation of Low-Peaking Satellite Observations Using the Coupled Interface Framework. Mon. Wea. Rev., 148, 637–654, https://doi.org/10.1175/MWR-D-19-0029.1.

12. Gaiser, P. W., and Coauthors, 2004: The WindSat spaceborne polarimetric microwave radiometer: Sensor description and early orbit performance. IEEE Trans. Geosci. Remote Sens., 42, 2347–2361.

13. Geer, A. J., P. Bauer, and P. Lopez, 2010: Direct 4D-Var assimilation of all-sky radiances. Part II: Assessment. Quarterly Journal of the Royal Meteorological Society, 136, 1886-1905.

14. Geer, A. J., 2019: Correlated observation error models for assimilating all-sky infrared radiances. Atmospheric Measurement Techniques, 12, 3629-3657.

15. Hogan, T. F., Liu, M., Ridout, J., Peng, M., Whitcomb, T., Ruston, B., et al. (2014). The Navy Global Environmental Model. Oceanography, 27(3), 116-125. https://doi.org/10.5670/oceanog.2014.73.

16. Langland, R. H., and Baker, N. L. (2004). Estimation of observation impact using the NRL atmospheric variational data assimilation adjoint system. Tellus A: Dynamic Meteorology and Oceanography, 56(3), 189–201. https://doi.org/10.3402/tellusa.v56i3.14413.

17. Le Marshall, J., Bi L., Jung J., Zapotocny T., and Morgan M., 2007: WindSat polarimetric microwave observations improve Southern Hemisphere numerical weather prediction. Aust. Meteor. Mag., 56, 35–40.

18. Kuhl, D. D., T. E. Rosmond, C. H. Bishop, J. McLay, and N. L. Baker, 2013: Comparison of hybrid ensemble/4DVar and 4DVar within the NAVDAS-AR data assimilation framework. Monthly Weather Review, 141, 2740-2758.

19. Reising, S., Chandrasekar, V., Kummerow, C., et al. 2021: Small Satellite Constellations: TEMPEST-D Demonstration of the Potential to Enable Temporal Observations of Cloud and Precipitation Processes. AGU Fall Meeting, New Orleans, LA.
20. Rosmond, T., and L. Xu, 2006: Development of NAVDAS-AR: Non-linear formulation and outer loop tests. Tellus, Series A: Dynamic Meteorology and Oceanography, 58, 45-58.
21. Stone, R. E., C. A. Reynolds, J. D. Doyle, R. H. Langland, N. L. Baker, D. A. Lavers, and F. M. Ralph, 2020: Atmospheric river reconnaissance observation impact in the navy global forecast system. Monthly Weather Review, 148, 763-782.
22. Xu, L., T. Rosmond, and R. Daley, 2005: Development of NAVDAS-AR: formulation and initial tests of the linear problem. Tellus A: Dynamic Meteorology and Oceanography, 57, 546-559.
23. Zheng, G., J. Yang, and L. Ren, 2014: Retrieval Models of Water Vapor and Wet Tropospheric Path Delay for the HY-2A Calibration Microwave Radiometer. Journal of Atmospheric and Oceanic Technology, 31, 1516-1528.
24. Zhu, Y., J. Derber, A. Collard, D. Dee, R. Treadon, G. Gayno, and J. A. Jung, 2014: Enhanced radiance bias correction in the National Centers for Environmental Prediction's Gridpoint Statistical Interpolation data assimilation system. Quarterly Journal of the Royal Meteorological Society, 140, 1479-1492.